ACS APPLIED POLYMER MATERIALS

pubs.acs.org/acsapm Article

Designing Intrinsically Microporous Polymer (PIM-1) Microfibers with Tunable Morphology and Porosity via Controlling Solvent/Nonsolvent/Polymer Interactions

Siyao Wang, Kaihang Shi, Anurodh Tripathi, Ushno Chakraborty, Gregory N. Parsons,* and Saad A. Khan*

Cite This: https://dx.doi.org/10.1021/acsapm.0c00386 Read Online

ACCESS | Metrics & More | Article Recommendations | Supporting Information

ABSTRACT: In this study, we present the fabrication of fibers with tunable morphology and porosity from an intrinsically microporous polymer, PIM-1, using a simple one-step electrospinning technique. The method involves the dissolution of PIM-1 in a good solvent tetrahydrofuran (THF) and cosolvents composed of THF and a nonsolvent, either dimethylformamide (DMF) or toluene, for electrospinning without the requirement of post-treatments. Electrospun PIM-1 fibers obtained from THF and different cosolvents reveal unique variations in fiber morphology, starting from changes in fiber surface texture to cross-sectional shape and internal/external pores. The change in the cross-sectional shape from corrugated circles to ribbon-like dumbbells can be attributed primarily to a buckling instability, while phase separation induced by the nonsolvent can be used to explain the formation of a highly porous structure both on the fiber surface and in the fiber interior at different solvent/nonsolvent ratios. With an increase in toluene fraction, the surface pores become more developed, whereas the interior pores demonstrate a decrease in size and density due to the competing effects between phase separation and fiber solidification. The hierarchical porosity of the fiber mats that comes from the macro (>50 nm) /meso pores (2−50 nm) created from nonsolvent induced phase separation (NIPS) during electrospinning and the intrinsic microporosity (<2 nm) from the PIM-1 rigid backbone contribute to an increase in the surface area of the fiber mats. These results are confirmed by nitrogen physisorption analysis and an improvement of CO_2 adsorptive capacity. CO_2 adsorption kinetics under different temperatures and adsorption/desorption cyclic stability investigated using a gravimetric approach show PIM-1 fiber mats to hold strong promise in applications for gas capture.

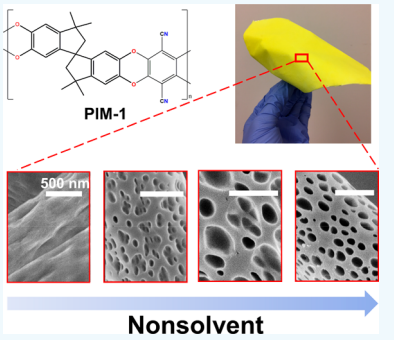

KEYWORDS: *polymer of intrinsic microporosity (PIM), buckling instability, cross-sectional shape, surface texture, nonsolvent induced phase separation (NIPS), hierarchical pores, electrospinning*

1. INTRODUCTION

Microporous materials have gained significant attention over the past few years in gas separation, energy storage, and heterogeneous catalysis owing to their large surface area, tunable pore architectures, and diverse functionalities.[1] Among them, polymers of intrinsic microporosity (PIMs), recently emerging as a novel subclass of microporous polymeric materials, have sparked considerable interest. PIMs possess a high surface area and interconnected micropores (<2 nm), which result from their rigid and contorted polymer backbone and inefficient chain packing.[2] A distinctive advantage of PIMs over other popular microporous materials such as zeolites, metal−organic frameworks (MOFs), or covalent−organic frameworks (COFs) is their solution processability in common organic solvents, which enables various physical forms that facilitate the effective use and possible applications of PIMs.[3] However, research on PIM materials has almost exclusively focused on dense flat sheet or thin film composite membrane morphologies.[4−9] Only a few recent studies demonstrate using other polymer processing techniques including wet spinning,[10−12] electrospinning,[13,14,23−25,15−22] and 3D printing,[26,27] among which electrospinning has been regarded as the most effective and versatile technology to produce micrometer−nanometer sized continuous fibers with controlled morphology and functionalities.[28−30]

Research on the use of electrospun PIMs has gathered momentum only in the past two−three years. Ferraris et al. first produced an electrospun PIM-1 fiber mat as an electrode for supercapacitors after carbonization.[14] Cao and co-workers prepared PIM/POSS (polyhedral oligomeric silsesquioxane) fibrous membranes for oil/water separation.[13] The same group

Received: April 11, 2020
Accepted: May 8, 2020
Published: May 8, 2020

also studied the adsorption of dyes from both nonaqueous and aqueous media by electrospun PIM-1[16] and hydrolyzed PIM-1 fibers,[17] respectively. However, in most of these studies, fibers were obtained using tetrachloroethane, which is a highly toxic solvent. To avoid the use of tetrachloroethane, Lasseuguette and Ferrari fabricated PIM-1 fibers by electrospinning with tetrahydrofuran and dimethylformamide.[15] Uyar and co-workers chemically modified the nitrile group on the PIM-1 backbone to make ultrafine fibers for various adsorption applications.[18,22,25] They also fabricated a chemically stable and mechanically robust nanofibrous membrane using hydrolyzed PIM-1/polybenzoxazine via thermal cross-linking.[19] Despite the promising performance of these electrospun fibers made from chemically modified PIM-1 in different adsorption studies, the post-synthesis step usually requires extended reaction hours and a large consumption of organic solvents. Modified PIM-1 often exhibits a reduction in porosity due to stronger interactions between polymer chains.[31] More importantly, fabricating, understanding, and exploiting the secondary morphologies of PIM fibers that can increase the porosity and expand the potential application fields is an area that remains largely unexplored.

For electrospun micro/nano fibers, in addition to smooth fibers with circular cross section, numerous fascinating secondary structures, including ribbon-like cross section,[32−34] a porous surface or core,[35−38] wrinkled surface,[34,39,40] and core−shell, hollow structures[41] were obtained in various studies. These hierarchical structures impart an additional surface area and other advantageous properties to the fibers that attract considerable interest. For instance, in oil cleanup processes, wrinkled or porous structures are excellent for enhancing the hydrophobic nature of the nonwoven material, allowing for superior selectivity of hydrocarbons.[38] Moreover, for faster adsorption kinetics, porous structures are developed with remarkable enhancements in surface area, which provide additional binding or adsorption sites.[38] However, to date, we have not found a paper focused on creating secondary morphologies on electropun PIM fibers. We believe that, by fabricating and understanding the secondary morphologies of PIM fibers, applications of PIM electrospun fibers could be further extended with improved fiber performance.

Among various secondary morphologies of electrospun fibers, generating macro pores (>50 nm) either on fiber surface or inside is attractive for numerous applications. Conventionally, the template technique and phase separation have been widely employed in this regard. For the template technique, porous fibers could be produced by selective removal of the sacrificial component;[42−45] however, a harsh post-treatment is usually required and complete removal of the sacrificial component is also challenging. The thermally induced phase separation (TIPS) method, where rapid solvent evaporation during electrospinning leads to temperature decrease and thermodynamic instability of the solution that induces phase separation, is a common way to generate porosity on electrospun fibers.[36,46] In the vapor-induced phase separation (VIPS) method, the electrospinning jet absorbs nonsolvent vapor (usually water) from the environment that causes the originally homogeneous solution to phase separate and porous structures can be obtained after the solvent removal.[47] In the nonsolvent induced phase separation (NIPS) approach, ternary systems containing a highly volatile solvent and a less volatile nonsolvent with different amounts premixed with the polymer are used to create porosity. During the subsequent solidification process, the composition changes and falls into the phase separation region due to the different volatility between the solvent and nonsolvent.[37,38,48,49] Compared to TIPS and VIPS, which require exquisite control of the environmental factors and mostly generate pores on the surface, pores throughout the fibers could be produced with NIPS with good reproducibility and ease of control.

In this study, we present for the first time, to the best of our knowledge, the incorporation of NIPS (nonsolvent induced phase separation) into the electrospinning process to produce PIM-1 fibrous mats with controlled morphology and hierarchical porosity. Fibers containing secondary structures are produced by a simple one-step electrospinning process from solutions composed of a good solvent, tetrahydrofuran (THF), and premixed THF with a nonsolvent, either dimethylformamide (DMF) or toluene. The difference in surface texture and cross-sectional shape of fibers electrospun from three solvent systems is correlated with solvent properties and explained in terms of a buckling instability. By further tuning the compositions of THF and toluene, fibrous mats with hierarchical porosity, ranging from macro (>50 nm) and meso (2−50 nm) pores generated by NIPS during electrospinning, and intrinsic micropores (<2 nm) resulted from rigid polymer backbone can be obtained. A fundamental study on pore formation mechanism is conducted by establishing ternary phase diagrams experimentally and theoretically. These porous features impart additional surface area to the fibrous mats and potentially extend the application of PIM fibers. As a demonstration, a mixture of CO_2/N_2 (15/85) is used to simulate flue gas. The temperature dependence of CO_2 adsorption and CO_2 adsorption/desorption cyclic stability show promise of these materials in gas capture.

2. EXPERIMENTAL SECTION

2.1. Materials. 5,5′,6,6′-Tetrahydroxy-3,3,3′,3′-tetramethyl-1,1′-spirobisindane (TTSBI, Alfa Aesar) was purified by reprecipitation from hot methanol with dichloromethane. Anhydrous potassium carbonate (Fisher Scientific) was crushed and dried at 110 °C under a vacuum overnight before use. Anhydrous *N*,*N*-dimethylformamide (DMF, Sigma-Aldrich) was stored over 4 Å molecular sieves prior to use. Tetrafluoroterephthalonitrile (TFTPN, Sigma-Aldrich), tetrahydrofuran (THF, Fisher Scientific), and anhydrous toluene (Fisher Scientific) were used as received.

2.2. Synthesis of PIM-1. PIM-1 was synthesized via low-temperature polycondensation of TFTPN and TTSBI.[50] All glassware was dried at 110 °C in an oven prior to use. TFTPN (3.0 g, 15 mmol) and TTSBI (5.1 g, 15 mmol) were added to anhydrous DMF (100 mL) in a 250 mL three-neck round-bottom flask under an inert atmosphere of nitrogen. The mixture was stirred at 65 °C until complete dissolution of both monomers. Potassium carbonate (5.1 g, 2.5 equiv) was then added to this solution. The reaction mixture was stirred under a nitrogen atmosphere at 65 °C for 72 h; it was then cooled to room temperature with DI water (300 mL) added to quench the reaction and precipitate the polymer. The precipitate was collected by vacuum filtration and washed with more DI water (500 mL) to remove any undissolved salts. The crude polymer was then dissolved in chloroform (120 mL) and reprecipitated using methanol (500 mL) to remove both the unreacted monomers and the oligomers. The precipitated product was then collected by vacuum filtration and dried in an oven at 110 °C overnight until completely dry, with a yield of 85%−90%. Figure S1 shows characterization of the PIM-1 obtained in terms of NMR, FTIR, and TGA.

2.3. Electrospinning of PIM-1. To prepare the solutions for electrospinning, PIM-1 powder was dissolved in THF and cosolvents of THF/toluene and THF/DMF at different ratios, followed by magnetic stirring at room temperature for 12 h to obtain

https://dx.doi.org/10.1021/acsapm.0c00386
ACS Appl. Polym. Mater. XXXX, XXX, XXX−XXX

homogeneous solutions. The polymer solutions were fed into a syringe pump (New Era Pump System Inc.) connected to a metallic needle (22 gauge, Hamilton), with a feed rate of 1−2 mL/h. The metallic needle was connected to a high-voltage power supply (Precision Inc.), and a grounded drum covered by a piece of aluminum foil was used as the fiber collector. The distance from the needle tip to the collector and the voltage were set at 15 cm and 10−15 kV, respectively. All the experiments were carried out at room temperature (20 ± 1 °C) and a relative humidity of 30 ± 3%. Humidity control was achieved by purging compressed air through anhydrous calcium sulfate (Drierite) in the electrospinning chamber. The sample codes of the electrospun fibers named for the compositions of the corresponding solutions are listed in Table 1.

Table 1. Solution Composition and Average Diameter of As-Spun Fibers

sample[a]	PIM-1 (mg/mL)	THF (% volume)	DMF (% volume)	toluene (T) (% volume)	fiber diameter[b] (μm)
T0	50	100	0	0	1.81 ± 0.26
T1	50	90	0	10	2.02 ± 0.44
T2	50	80	0	20	2.50 ± 0.36
T3	50	70	0	30	4.08 ± 0.55
T4	50	60	0	40	4.63 ± 0.45
D1	50	90	10	0	1.54 ± 0.15

[a]In the alphanumeric nomenclature, the alphabet represents the nonsolvent, whereas 10 times the number corresponds to its volume percent. [b]The diameters of electrospun PIM-1 fibers are defined as the widest dimension from the cross-sectional image.

2.4. Characterization Methods. The morphologies of the as-spun fibers were characterized by a field emission scanning electron microscope (FEI, Verios 490L). SEM images were captured at an accelerating voltage of 2 kV. For cross-sectional imaging, the polymer fibers were fractured in liquid N_2 using a sharp clean blade. The samples were sputter-coated with a 7 nm layer of gold and palladium before imaging. The diameters of electrospun PIM-1 fibers were defined as the widest dimension from the cross-sectional image and were quantified using ImageJ software by measuring ∼20 different fibers for each. The N_2 adsorption and desorption isotherms were obtained at 77 K using Micromeritics 3Flex. The Brunauer−Emmett−Teller (BET) surface area was calculated from N_2 adsorption isotherm between the relative pressures of 0.01−0.1. Reported BET surface area was averaged from three repeated tests with ±10 m^2/g experimental uncertainty. CO_2 adsorption and desorption isotherms were obtained at 273 K following a similar procedure. Before analysis, all samples were degassed at 110 °C for 12 h to remove any absorbed species. For the fiber samples in this study, the samples were refreshed by methanol to eliminate any confounding aging effects before each measurement.[51] CO_2 adsorption kinetics under different temperatures and adsorption/desorption cycling experiments were performed with a TA Instruments SDT 650. In a typical test, a 5−10 mg fiber sample was pretreated to 110 °C at 10 °C/min under N_2 (99.999%) with a flow rate of 100 mL/min and held for 60 min to remove any adsorbed species. The samples were then cooled to the analysis temperature and equilibrated for 60 min. Subsequently, the gas flow was switched to 15% CO_2 /N_2 (Acro) with a flow rate of 150 mL/min for 30 min. Cyclic stability experiments were performed following similar procedures described above except the isothermal temperature for degassing and equilibrating were both 30 min instead.

2.5. Construction of Ternary Phase Diagram. The ternary phase diagrams for PIM-1/THF/toluene and PIM-1/THF/DMF were determined by both experimental cloud point measurements and theoretical calculations based on the Flory−Huggins model (detailed information provided in Section 6, Supporting Information). The cloud point test was conducted in a homemade turbidity measurement device (Figure S3), consisting of a green laser diode featuring a wavelength λ = 560 nm as light source, a 3D printed sample holder, and a photodiode (Shine Gold Electronics) with a spectral response range from 390 to 675 nm and peak sensitivity wavelength of 565 nm for light detection. A series of polymer solutions with different PIM-1 concentrations (2.5%, 5%, 10%, 15%, and 20% m/v) in THF was prepared. Upon full dissolution, the nonsolvent, either toluene or DMF, was added dropwise under constant vigorous stirring. The solution would then transform from a clear homogeneous solution to a cloudy solution at a certain point. The transmittance of the system, which was reflected by the output signal of voltage, was monitored continuously during the experiment. Note that local turbidity happened immediately at the interface of the titrated nonsolvents and the PIM-1/THF solution. Further stirring of the solution for several minutes to a few hours was needed in order to achieve the bulk equilibrium condition, indicated by the stable transmittance signal. The amount of nonsolvent was continuously increased until the transmittance decrease was observed at equilibrium. The composition at the onset of transmittance decrease was recorded and provided one point on the binodal curve.

3. RESULTS AND DISCUSSION

3.1. Electrospun PIM-1 Microfibers. PIM-1 microfibers were electrospun from three different cosolvent systems: THF, THF/DMF, and THF/toluene. Among those three solvents, THF is a good solvent for PIM-1. DMF and toluene are two nonsolvents exploited here to develop hierarchical structure in the fiber. To be noted, DMF and toluene both have a swelling effect on PIM-1.[52,53] We use the term "nonsolvent" here as a comparison to the "solvent" THF, in which the polymer dissolves instantaneously. Table 1 depicts the solvent compositions used in our study; in almost all cases, the concentration of PIM-1 was kept constant at 5% w/v. The THF/toluene solvent ratio was adjusted from having no toluene (100% THF), T0, to 40% toluene, T4, in increments of 10% by volume (e.g., T1 with 10% toluene, T2 with 20% toluene). D1 stands for fibers electrospun using THF and DMF with 10% DMF. Figure 1 shows the chemical structure of PIM-1 and the as-spun PIM-1 fiber mat obtained from THF only (T0). As shown in the photographs, the resulting fiber mat appears uniform, flexible, and robust for laboratory handling.

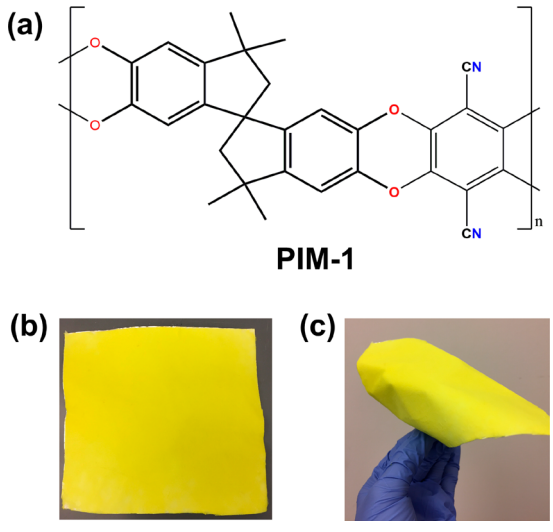

Figure 1. (a) Chemical structure of PIM-1. PIM-1 electrospun fiber mat (b) on top of an aluminum foil revealing its uniformity and (c) showing its flexibility.

https://dx.doi.org/10.1021/acsapm.0c00386
ACS Appl. Polym. Mater. XXXX, XXX, XXX−XXX

3.2. Effect of Different Solvent Systems on Fiber Morphology. The SEM images of as-spun PIM-1 fibers in different solvent systems and their cross sections are shown in Figure 2. T0 fibers exhibited a wrinkled surface with a diameter

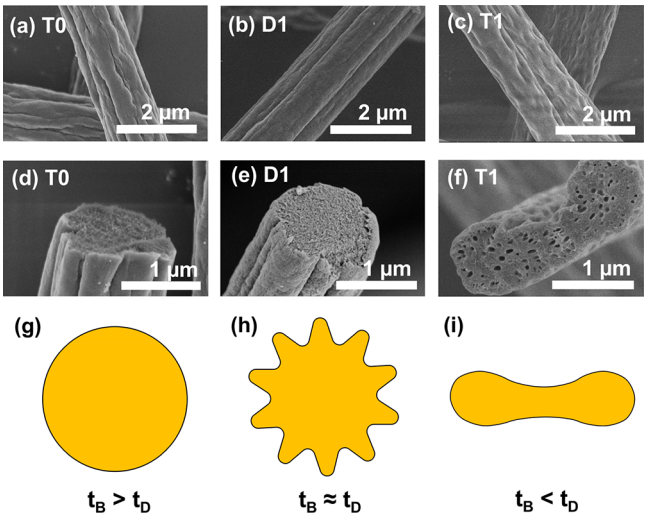

Figure 2. Representative SEM micrographs of (a–c) the surfaces and (d–f) the cross sections of the as-spun PIM-1 microfibers fabricated from solutions with varying compositions. (g–i) Schematic representation of cross-sectional shapes.

of ~1.8 μm (Figure 2a). The addition of 10% DMF as the cosolvent smoothened the fiber (D1), showing a few grooves on fiber surface along the fiber axis, and reduced the fiber diameter to 1.54 μm (Figure 2b). If the cosolvent is replaced by 10% toluene, T1 fibers exhibit ellipse-shaped dimples randomly distributed on the surface of approximately 400 nm in length (Figure 2c). The T1 fibers are flat in shape with a width around 2.02 μm. In terms of fiber cross sections shown in the bottom SEM images of Figure 2, both T0 and D1 fibers exhibited circular cross sections (Figure 2d,e). However, T1 fibers exhibited a dumbbell-shaped ribbon-like cross section (Figure 2f). The difference in surface features and cross-sectional shapes of fibers electrospun from three solvent systems indicates that solvent properties play a significant role in determining fiber morphology. Low-magnification SEM images of the as-spun fibers are shown in Figure S2. Uniform fibrous morphology is demonstrated for T0, T1, and D1 fibers in Figure S2a–c).

3.3. Buckling Instability and Fiber Shape. To understand the effect of different solvents on fiber shape, we introduce the concept of a buckling instability, which is associated with the formation of a thin glassy skin on the surface of a fluid during solvent evaporation.[40,54,55] Specifically, solvent evaporation and drying lead to the rapid formation of a hard elastic shell on the outside of the spinning jet. Due to continued evaporation of solvent from the core, there will be a contraction mismatch between the core and shell. At a critical compressive stress, the shell starts to buckle instead of enduring a uniform circumferential compression to minimize the energy consumption. Pauchard et al. observed a similar phenomenon as a result of solvent evaporation from a sessile droplet of polymer solution. Their analysis identified two characteristic times, drying time t_D and the buckling time t_B. A collapse may be observed if the buckling time is reached before the drying time ($t_B < t_D$).[55] Rutledge et al. also extended this concept of balanced drying and buckling kinetics to electrospun fibers.[34]

In this study, the observed fiber surface texture and cross-sectional shape appear to be consistent with buckling phenomena. In this case, for $t_B > t_D$, solidification of the polymer jet would occur before any buckling instability, leading to a cylindrical morphology, as shown Figure 2g. If t_B is comparable to t_D, the morphology would resemble that shown in Figure 2h. For $t_B < t_D$, the onset of buckling instability would occur prior to solidification, resulting in a shape similar to that shown in Figure 2i. The difference between b and c depends on the critical buckling wavenumber and wavelength, which leads to lowest total energy.[40] For our fibers, we observed two of these three scenarios shown in Figure 2(g–i). Fibers electrospun from THF alone (T0) show a wrinkled surface with a cross-sectional shape that resembles Figure 2h. The rapid evaporation of the highly volatile THF facilitates skin layer formation and triggers buckling instability while concurrently also aiding drying, possibly leading to a case of comparable t_B and t_D. The D1 fibers electrospun from a cosolvent of THF and DMF exhibit similar cross sections as T0 fibers, with the wrinkles on the fiber surfaces further stretched into grooves. The addition of low-volatility DMF as the cosolvent may increase the drying time of the spinning jet. However, a high-dielectric constant coupled with good conductivity of DMF (Table 2) greatly enhances the electrostatic repulsion loaded on jet surface, which eventually contributes to a rapid solidification due to reduced surface area under high stretching.[56−60] For fibers formed using toluene as a cosolvent with THF (T1), we observed ribbon-like shapes resembling Figure 2i. The extremely low conductivity of toluene along with its low-dielectric constant significantly extends the drying time of the jet, causing the skin layer to collapse and form the concave ribbon shapes. It should be noted that D1 fibers have the smallest diameter of 1.54 μm due to the high stretching, while the T1 fibers have the largest diameter of around 2.02 μm because of the lowest stretching.

The drying time, and consequently the fiber shape, can also be altered by changing the precursor polymer concentration. This is illustrated in Figure 3a, which shows the contour and the cross section of a fiber obtained from a solution containing 7.5 wt % PIM-1 in THF. Upon increasing the polymer concentration, the electrospinning jet experiences a longer drying time due to a stronger interaction between the polymer and solvent and a reduced buckling time due to a smaller

Table 2. Different Properties of the Solvents Used in Our Study[a]

solvent	boiling point (°C)	viscosity (25 °C, cP)	conductivity (S m^{-1})	dielectric constant (20 °C)	surface tension (20 °C, 10^{-3}N m^{-1})
THF	66	0.55	4.5×10^{-5}	7.6	28
DMF	153	0.82	6.0×10^{-8}	36.7	35
toluene	110.6	0.59	8.0×10^{-16}	2.38	28.5

[a]Data reported in this table have been taken from ref 61.

https://dx.doi.org/10.1021/acsapm.0c00386
ACS Appl. Polym. Mater. XXXX, XXX, XXX−XXX

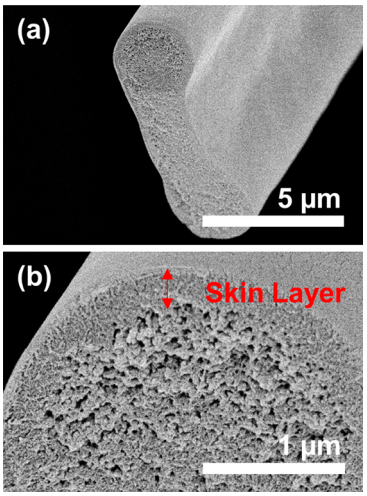

Figure 3. Cross-sectional image of PIM-1 microfiber obtained from a precursor solution of 7.5 wt % PIM-1 in THF showing (a) dumbbell-like fiber shape and (b) internal microstructure of cross section at a higher magnification.

polymer concentration gradient between the fiber surface and the core.[34] Hence, a flat ribbon cross section is observed with a loose structure in the core surrounded by a ~800 nm dense skin layer (Figure 3b).

3.4. Effect of Solvent/Nonsolvent Ratios on Fiber Porosity. The unique fiber morphologies obtained, such as seen in fiber T1 (Figure 2c,f) with surface dimples and pores in cross section, prompted us to investigate further the role of solvent composition on fiber topology and internal structure. Figure 4 shows SEM images of PIM-1 fibers electrospun from cosolvents of THF and toluene containing 10%, 20%, 30%, and 40% of toluene represented by T1, T2, T3, and T4, respectively. Several phenomena were observed on the electrospun fiber surface as the toluene fraction increased

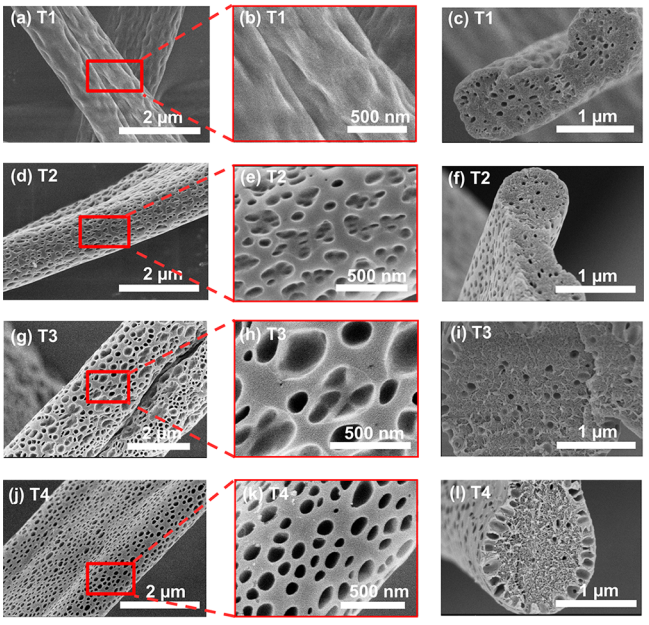

Figure 4. (a, d, g, j) SEM micrographs of the surfaces with (b, e, h, k) a higher magnification and (c, f, i, l) cross sections of T1, T2, T3, and T4 PIM-1 microfibers.

from 10% to 40%. First, the randomly distributed elliptical dimples oriented along the fiber axis (T1, Figure 4a,b) with a length of 500−800 nm were transformed to heavily populated small pits on the fiber surface that were 60−90 nm in length and 30−50 nm in width perpendicular to the fiber axis (T2, Figure 4d,e) as the toluene fraction increased from 10% to 20%. Second, upon further increasing the toluene fraction, the surface pits were significantly enlarged with reduced degree of pit coalescence (T3, Figure 4g,h). The average pore size was in the order of 150−200 nm in length and 80−120 nm in width. Finally, at 40% toluene fraction, fully developed slightly elliptical pores were observed that were uniformly distributed on the fiber surface (T4, Figure 4j,k). Pore lengths were in the range of 130−150 nm and widths were in the range of 80−100 nm. It is apparent that the surface morphology and pore size of PIM-1 fibers are highly dependent on the toluene fraction in the cosolvents, indicating that the nonsolvent must play an important role in the pore formation. Moreover, as the polymer jets experience dramatic elongation due to the electrostatic repulsion during electrospinning, the shape and orientation of the pores are affected by these stretching forces at the same time.

The cross sections of the fibers are shown in the third column of Figure 4. T1 fibers exhibit abundant pores in the fiber interior, with circular pores in the two ends and elliptical ones in the middle (Figure 4c). The pore size was in the range 60−90 nm in diameter for the circular ones and in length for the elliptical ones. The density of the pores was around 30−40 per fiber cross section. As the toluene fraction increased to 20%, a distinctive reduction in both pore size and pore density was observed (Figure 4f). The average pore size was approximately 40−60 nm, with the number of pores reduced to 20−30 per fiber. With more toluene in the cosolvent, T3 fibers showed similar pore size and density as T2 fibers, but interestingly, pores on the surface began to protrude into the core with a 100−120 nm depth (Figure 4i). When the toluene fraction reached 40%, the size of the interior pores did not change much and the density of the pores was reduced to less than 10 per cross section (Figure 4l). More importantly, the surface pores further grew into the core with an increased depth of 180−200 nm, densely packed underneath the fiber surface. This suggests that the holes formed inside the fibers are closely related to the amount of the nonsolvent as well, but the different trend in pore morphology evolution indicates that the surface pores and interior pores are formed under different mechanisms, which are discussed in the following section.

3.5. Nonsolvent Induced Phase Separation (NIPS). During the electrospinning process, significant elongation of the spinning jet resulting from electrostatic repulsion of the charges on fiber surface leads to a dramatic increase of the jet surface area within milliseconds, which greatly accelerates the evaporation of both solvent and nonsolvent simultaneously. Because THF has a much higher vapor pressure than the nonsolvent toluene, the jet becomes compositionally unstable due to the increase of nonsolvent fraction. Thus, the effect of phase separation needs to be considered. Conventionally, ternary phase diagrams like the one shown in Figure 5 are used to explain NIPS and have been utilized to examine membrane formation,[54] wet spinning,[62,63] and 3D printing.[26] Briefly, the phase diagram is divided into three regions by the binodal and spinodal curves: stable, unstable, and metastable. The three components coexist in the stable region I and phase separate in the metastable region II between the binodal and spinodal

https://dx.doi.org/10.1021/acsapm.0c00386
ACS Appl. Polym. Mater. XXXX, XXX, XXX−XXX

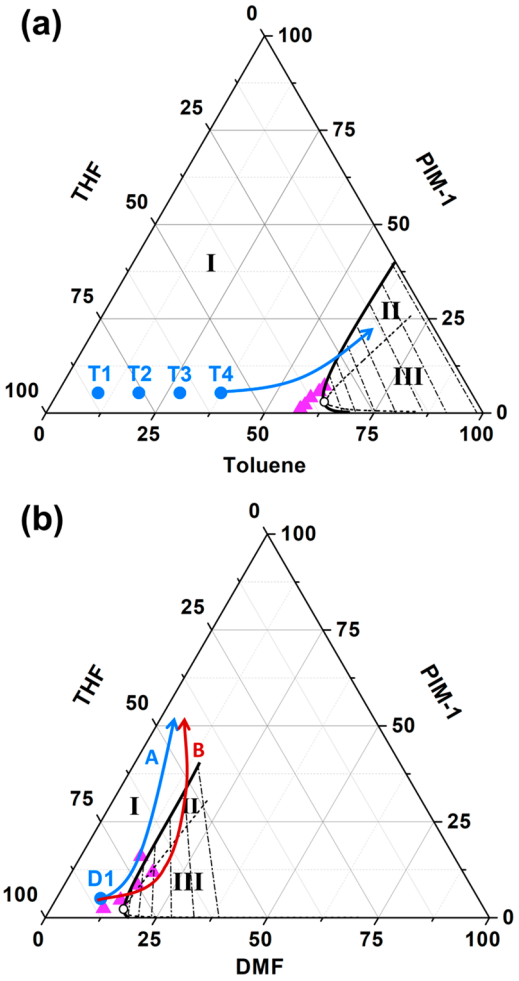

Figure 5. Ternary phase diagrams of PIM-1/THF/nonsolvent system at 295.15 K: (a) toluene and (b) DMF. Theoretical predictions for the binodal curves (solid lines), spinodal curves (dashed lines), tie lines (dash-dotted lines), and critical points (open circles) are plotted against experimental cloud points for the choice of nonsolvent to be DMF and toluene (purple triangles). Arrows are proposed composition paths.

curves and the unstable region III covered by spinodal curve. It is well-known that the polymer phase separates via nucleation and growth (NG) in the metastable region, whereas spinodal decomposition (SD) occurs in the unstable region. Generally, an open-cell or interconnected network structure is produced by SD, while closed, isolated pores are characteristic of NG.[62] The final morphology is determined by the competition between drying rate and phase separation rate.

To understand the mechanism for the pore formation on fiber surface and in the interior, we examined the phase behaviors of PIM-1/THF/toluene ternary system both experimentally by the cloud point method and theoretically by calculations based on the Flory–Huggins model as complementary confirmation (Section 5, Supporting Information), as shown in Figure 5a. The initial compositions of polymer solutions with different toluene fractions are indicated by blue solid circles. The arrow represents how the composition of polymer solution may change under competing effect between fiber solidification and phase separation. Specifically, as the faster evaporation of THF increases the fraction of nonsolvent (toluene) in solutions, the composition of the spinning jet falls in the unstable region and phase separated structure sets in. With a low fraction of toluene in the cosolvent (e.g., T1), there is a large gap between the initial composition and the binodal demixing curve. As a result, the jet surface composition takes a longer time to cross the binodal curve and surface texture sets in at an early stage of phase separation, leaving the randomly distributed dimples on the surface. As the toluene fraction increases, phase separation on jet surface starts earlier. Small pores appear on the surface of T2 fibers and start merging with each other until fully developed pores are observed in T4. Because of the elongation in the axial direction under stretching, the domains are oriented along the fiber axis and deformed into ellipsoid on the surface. Meanwhile, in the jet interior, THF evaporates slower compared to on the surface. With a high THF fraction in the cosolvent (e.g., T1), interior pores have enough time to grow/ripe before the jet solidifies. With less THF (more toluene), morphology sets in earlier, leading to a reduction in pore size and density from T1 to T4. The pores are spherical initially to reduce interfacial free energy until the collapse of the fiber skin layer under buckling instability deforms them into elliptical shapes.

Solvent properties also play a role in the competition between the drying and phase separation rates. Figure 5b shows that DMF would induce a higher tendency of phase separation than toluene, as the binodal curve is closer to the polymer solvent axis for DMF than for toluene. At a fixed solvent/nonsolvent ratio of 9:1, it is much easier for PIM-1 solution with DMF as nonsolvent to pass the liquid–liquid demixing line. However, as observed from Figure 2e, neither surface nor interior pores appear on sample D1. This could be explained by the significantly higher dielectric constant of DMF compared to that of toluene (Table 2). The jet with DMF would experience much larger stretching from electrostatic repulsion of charges on the jet surface, accelerating the evaporation rate of both the solvent and nonsolvent. As a result, on one hand, the elevated diffusivity of solvent and nonsolvent will reduce the difference of the evaporation rate of the two components, making it more difficult to pass the binodal curve and follow path A in Figure 5b. On the other hand, the phase separation induced structure may not have enough time to develop even with the composition entering the two-phase region, following path B in Figure 5b.[37]

3.6. Surface Area and CO_2 Adsorption Performance.

Given the varied and hierarchical structures of the fibers, we attempted to quantify the porosity and gas sorption performance of the fibers with surface and inside pores by acquiring nitrogen and CO_2 physisorption isotherms. Table S1 summarizes the calculated surface area, total pore volume (@ P/P0 = 0.95) and the amount of adsorbed CO_2 (@ 273 K, 1 bar) for all samples. Figure 6a,b shows physisorption isotherms at 77K of T1–T4 fibers along with the pristine PIM-1 powder. We observed comparable surface area for some of the fibers (e.g., T4, Figure 6b) to the PIM-1 powder as well reduced surface area (e.g., T0, T1, D1, T2, Table S1) depending on the nature of the microstructure of the fibers. Literature studies[16,20,21] reveal variation in the values of the surface area measurements of PIM-1 powder as well as its trend with the area of the corresponding fibers. An understanding of the disparity in surface area values as well as the differences between fiber and powders could be an area of future research. However, this is outside the scope and purpose of this work. We surmise that the reduction observed

https://dx.doi.org/10.1021/acsapm.0c00386
ACS Appl. Polym. Mater. XXXX, XXX, XXX–XXX

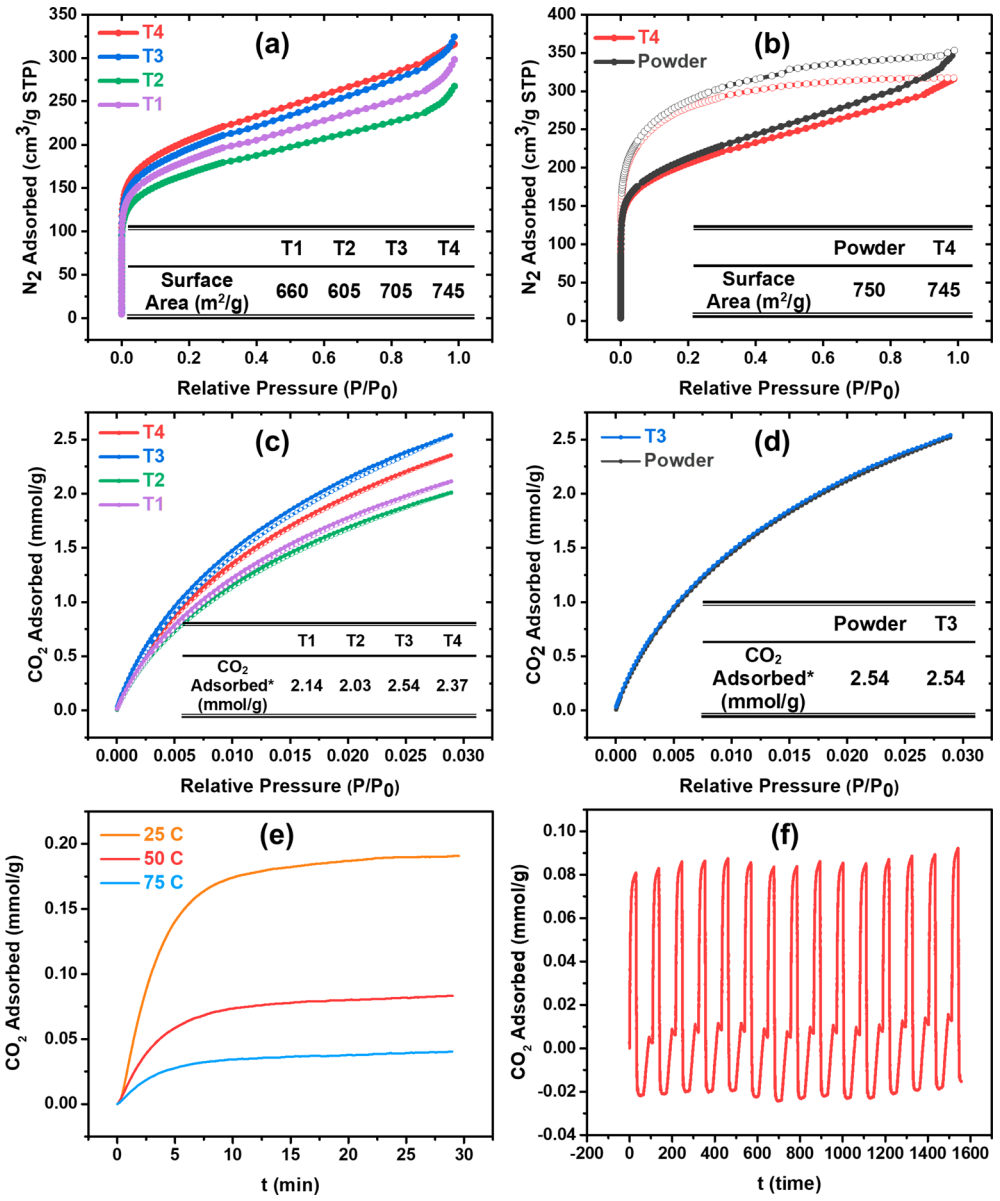

Figure 6. Nitrogen adsorption/desorption isotherms at 77K of (a) T4, T3, T2, and T1 fibers and (b) PIM-1 powder and T4 fibers. CO_2 adsorption/desorption isotherms at 273 K of (c) T4, T3, T2, and T1 fibers and (d) PIM-1 powder and T3 fibers. Adsorption: closed symbols. Desorption: open symbols. *CO_2 adsorbed amount at 273 K, 1 bar. (e) CO_2 uptake of T3 fibers at 25, 50, and 75 °C, and (f) cyclic CO_2 adsorption/desorption performance at 50 °C using CO_2/N_2 (15/85) via a gravimetric method. The adsorbed CO_2 was normalized to 0 at 50 °C under a N_2 flow.

in some of our samples may be related to the fact that total surface area comprises both micropores intrinsic to the polymer structure and mesopores dependent on the physical morphology. In our case, the extra void space of PIM-1 powder from random precipitation decreases during processing due to polymer chain orientation. In addition, the decreased mesoporosity may also make some micropores[64] inaccessible and difficult to be detected. The pore size distribution (PSD) was acquired from a smooth shift nonlocal density functional theory (SSNLDFT) method developed by the Colina group[65] (Figure S4). From Figure S4c,d, we observed that all the fiber samples maintained the microporosity from PIM-1 powder (Figure S4b), as we surmised earlier while discussing Table S1.

The CO_2 adsorption and desorption isotherms of PIM fibers at 273 K are shown in Figure 6c,d. All isotherms show the dual-mode behavior, which is typical of glassy polymers.[66] Similar to nitrogen physisorption, T3 and T4 fibers with hierarchical porosity demonstrate a distinctive increase in CO_2 adsorption relative to T2 and T1 fibers at low pressures, in which T3 fibers exhibit CO_2 adsorption performance close to that of PIM powder. We believe that the macro/mesoporosity generated by phase separation along with the much higher kinetic energy of CO_2 molecules at 273 K contribute to increased accessibility of isolated micropores from the polymer and eventually lead to an increased adsorption capacity of the fiber mats. To be noted, the CO_2 adsorption capacity of T3 fibers is prominent among physisorption based solid sorbents for CO_2.[67] The fibrous morphology of the sorbent also brings in an extra benefit when compared to powder sorbent, e.g., a reduced pressure drop.[66]

To further demonstrate the potential of PIM-1 fibers in gas capture, we selected T3 fibers to examine CO_2/N_2 binary gas

https://dx.doi.org/10.1021/acsapm.0c00386
ACS Appl. Polym. Mater. XXXX, XXX, XXX−XXX

sorption performance via a gravimetric approach. A mixture of CO_2 /N_2 (15/85) was used to simulate the major component of flue gas. Figure 6e shows CO_2 adsorption performance under three different temperatures: 25, 50, and 75 °C. We observed that with the increase in temperature, there is a decrease in CO_2 adsorption capacity, confirming the exothermic nature of the adsorption process. The adsorption kinetics was investigated by fitting the experimental data to both a linear and quadratic driving force models[68,69] (Figure S5). The linear driving force model fits the experimental data well at lower temperatures, while quadratic driving force model fits better at higher temperatures, indicating stronger interactions between CO_2 and the nitrile groups on PIM-1 backbone at higher temperatures. The kinetic constants are summarized in Tables S2 and S3. The rate constants obtained from the first order model fit are nearly independent of temperature (Table S2), whereas the kinetic constants from second order model fit increase with temperature. These model dependent numbers are consistent with what is observed in the literature. More importantly, the mats reach their equilibrated capacity in less than 10 min, analogous to what is observed in other used systems such as activated carbon. The CO_2 adsorption/desorption cycling stability at 50 °C is shown in Figure 6f. The as-fabricated fibers demonstrate excellent cycling stability with no observable loss in capacity within 15 cycles, suggesting their potential to remove CO_2 from flue gas at elevated temperatures.

4. CONCLUSIONS

In this work, we successfully fabricated PIM-1 microfibers with controlled morphology and porosity by a simple one-step electrospinning process. Different secondary morphologies including fiber surface texture and cross-sectional shape were obtained when electrospun from three solvent systems, including a good solvent THF and THF premixed with a nonsolvent, either DMF or toluene. We found that the formation of these secondary morphologies are highly related to solvent properties and can be explained by applying a concept of buckling instability. Motivated by the unique feature from fibers electrospun from THF/toluene, we further investigated the effect of solvent/nonsolvent ratio on fiber morphology. Porous structures, both on the fiber surface and interior were produced, with the surface pores becoming more developed and interior pores shrinking in size and density as the toluene fraction increased. To explain the pore formation mechanism, ternary phase diagrams were established both experimentally and theoretically. We found that pores were formed under nonsolvent induced phase separation with the final fiber morphology being determined by the competing effects between phase separation and fiber solidification. The hierarchical porosity of the fiber mats that comes from the macro pores created from NIPS during electrospinning and the intrinsic microporosity from PIM-1 rigid backbone contributed to an increase in the surface area of the fiber mat, as confirmed by nitrogen physisorption analysis and an improvement of CO_2 adsorptive capacity. CO_2 uptake under three different temperatures were investigated using a mixture of CO_2/N_2 (15/85) to mimic flue gas. CO_2 adsorption kinetics showed that systems reached equilibrated values in a short period of time, while the values decreased with increased temperature. As-made fibers also demonstrated excellent adsorption/desorption stability over 15 cycles under 50 °C. These results indicate the potential of using PIM-1 fiber mats for gas capture. Moreover, the size of the surface pores can be easily controlled by changing the fraction of good solvents and nonsolvents, rendering this electrospinning process a simple method to fabricate porous fiber mats for tailored applications.

ASSOCIATED CONTENT

Supporting Information

The Supporting Information is available free of charge at https://pubs.acs.org/doi/10.1021/acsapm.0c00386.

Discussions of characterization and bulk polymer properties, kinetics of CO_2 adsorption, and ternary phase diagram calculation details, figures of ^{1}H NMR spectra, FTIR spectra, TGA curves, molecular weight distribution, optical images, SEM images, experimental setup for cloud point measurement, nitrogen adsorption/desorption isotherms, pore size distribution, and CO_2 adsorption plots, and tables of surface area, pore volume, and quantity of adsorbed CO_2, linear and quadratic driving force mass transfer coefficients at different temperatures and the corresponding adsorption capacities, and parameters required by Flory−Huggins theory (PDF)

AUTHOR INFORMATION

Corresponding Authors

Gregory N. Parsons − *Department of Chemical and Biomolecular Engineering, North Carolina State University, Raleigh, North Carolina 27695, United States;* orcid.org/0000-0002-0048-5859; Email: gnp@ncsu.edu

Saad A. Khan − *Department of Chemical and Biomolecular Engineering, North Carolina State University, Raleigh, North Carolina 27695, United States;* orcid.org/0000-0002-1530-8249; Email: khan@eos.ncsu.ed

Authors

Siyao Wang − *Department of Chemical and Biomolecular Engineering, North Carolina State University, Raleigh, North Carolina 27695, United States*

Kaihang Shi − *Department of Chemical and Biomolecular Engineering, North Carolina State University, Raleigh, North Carolina 27695, United States*

Anurodh Tripathi − *Department of Chemical and Biomolecular Engineering, North Carolina State University, Raleigh, North Carolina 27695, United States;* orcid.org/0000-0002-3415-0221

Ushno Chakraborty − *Department of Chemical and Biomolecular Engineering, North Carolina State University, Raleigh, North Carolina 27695, United States*

Complete contact information is available at: https://pubs.acs.org/10.1021/acsapm.0c00386

Notes

The authors declare no competing financial interest.

ACKNOWLEDGMENTS

The authors gratefully acknowledge the support of the Nonwovens Institute (NWI) at North Carolina State University for funding this work. This work was performed in part at the Analytical Instrumentation Facility (AIF) at North Carolina State University, which is supported by the State of North Carolina and the National Science Foundation (award number ECCS-1542015). The AIF is a member of the

North Carolina Research Triangle Nanotechnology Network (RTNN), a site in the National Nanotechnology Coordinated Infrastructure (NNCI). The authors would also like to thank Mike Mantini for his help in constructing the experimental set up for cloud point measurement, Dr. Pandiyarajan Chinnayan Kannan for helpful discussions on monomer purification and PIM-1 synthesis, Yeongun Ko for help on GPC characterization, and Ryan Dudek for help with the TGA measurements.

REFERENCES

(1) Denny, M. S.; Moreton, J. C.; Benz, L.; Cohen, S. M. Metal−Organic Frameworks for Membrane-Based Separations. *Nat. Rev. Mater.* **2016**, *1* (12), 16078.
(2) Budd, P. M.; Elabas, E. S.; Ghanem, B. S.; Makhseed, S.; McKeown, N. B.; Msayib, K. J.; Tattershall, C. E.; Wang, D. Solution-Processed, Organophilic Membrane Derived from a Polymer of Intrinsic Microporosity. *Adv. Mater.* **2004**, *16* (5), 456−459.
(3) McKeown, N. B.; Budd, P. M.; Msayib, K. J.; Ghanem, B. S.; Kingston, H. J.; Tattershall, C. E.; Makhseed, S.; Reynolds, K. J.; Fritsch, D. Polymers of Intrinsic Microporosity (PIMs): Bridging the Void between Microporous and Polymeric Materials. *Chem. - Eur. J.* **2005**, *11* (9), 2610−2620.
(4) Ogieglo, W.; Furchner, A.; Ma, X.; Hazazi, K.; Alhazmi, A. T.; Pinnau, I. Thin Composite Carbon Molecular Sieve Membranes from a Polymer of Intrinsic Microporosity Precursor. *ACS Appl. Mater. Interfaces* **2019**, *11* (20), 18770−18781.
(5) Dong, G.; Zhang, J.; Wang, Z.; Wang, J.; Zhao, P.; Cao, X.; Zhang, Y. Interfacial Property Modulation of PIM-1 through Polydopamine-Derived Submicrospheres for Enhanced CO_2/N_2 Separation Performance. *ACS Appl. Mater. Interfaces* **2019**, *11* (21), 19613−19622.
(6) Hou, R.; Smith, S. J. D.; Wood, C. D.; Mulder, R. J.; Lau, C. H.; Wang, H.; Hill, M. R. Solvation Effects on the Permeation and Aging Performance of PIM-1-Based MMMs for Gas Separation. *ACS Appl. Mater. Interfaces* **2019**, *11* (6), 6502−6511.
(7) Ogieglo, W.; Ghanem, B.; Ma, X.; Wessling, M.; Pinnau, I. High-Pressure CO_2 Sorption in Polymers of Intrinsic Microporosity under Ultrathin Film Confinement. *ACS Appl. Mater. Interfaces* **2018**, *10* (13), 11369−11376.
(8) Benzaqui, M.; Semino, R.; Menguy, N.; Carn, F.; Kundu, T.; Guigner, J. M.; McKeown, N. B.; Msayib, K. J.; Carta, M.; Malpass-Evans, R.; Le Guillouzer, C.; Clet, G.; Ramsahye, N. A.; Serre, C.; Maurin, G.; Steunou, N. Toward an Understanding of the Microstructure and Interfacial Properties of PIMs/ZIF-8 Mixed Matrix Membranes. *ACS Appl. Mater. Interfaces* **2016**, *8* (40), 27311−27321.
(9) Fuoco, A.; Comesaña-Gándara, B.; Longo, M.; Esposito, E.; Monteleone, M.; Rose, I.; Bezzu, C. G.; Carta, M.; McKeown, N. B.; Jansen, J. C. Temperature Dependence of Gas Permeation and Diffusion in Triptycene-Based Ultrapermeable Polymers of Intrinsic Microporosity. *ACS Appl. Mater. Interfaces* **2018**, *10* (42), 36475−36482.
(10) Yong, W. F.; Li, F. Y.; Xiao, Y. C.; Chung, T. S.; Tong, Y. W. High Performance PIM-1/Matrimid Hollow Fiber Membranes. *J. Membr. Sci.* **2013**, *443*, 156−169.
(11) Hao, L.; Zuo, J.; Chung, T.-S. Formation of Defect-Free Polyetherimide/PIM-1 Hollow Fiber Membranes for Gas Separation. *AIChE J.* **2014**, *60* (11), 3848−3858.
(12) Jue, M. L.; Breedveld, V.; Lively, R. P. Defect-Free PIM-1 Hollow Fiber Membranes. *J. Membr. Sci.* **2017**, *530*, 33−41.
(13) Zhang, C.; Li, P.; Cao, B. Electrospun Microfibrous Membranes Based on PIM-1/POSS with High Oil Wettability for Separation of Oil−Water Mixtures and Cleanup of Oil Soluble Contaminants. *Ind. Eng. Chem. Res.* **2015**, *54* (35), 8772−8781.
(14) Bonso, J. S.; Kalaw, G. D.; Ferraris, J. P. High Surface Area Carbon Nanofibers Derived from Electrospun PIM-1 for Energy Storage Applications. *J. Mater. Chem. A* **2014**, *2* (2), 418−424.
(15) Lasseuguette, E.; Ferrari, M. Development of Microporous Electrospun PIM-1 Fibres. *Mater. Lett.* **2016**, *177*, 116−119.
(16) Zhang, C.; Li, P.; Cao, B. Electrospun Polymer of Intrinsic Microporosity Fibers and Their Use in the Adsorption of Contaminants from a Nonaqueous System. *J. Appl. Polym. Sci.* **2016**, *133* (22), 43475.
(17) Zhang, C.; Li, P.; Huang, W.; Cao, B. Chemical Engineering Research and Design Selective Adsorption and Separation of Organic Dyes in Aqueous Solutions by Hydrolyzed PIM-1 Microfibers. *Chem. Eng. Res. Des.* **2016**, *109*, 76−85.
(18) Satilmis, B.; Budd, P. M.; Uyar, T. Systematic Hydrolysis of PIM-1 and Electrospinning of Hydrolyzed PIM-1 Ultrafine Fibers for an Efficient Removal of Dye from Water. *React. Funct. Polym.* **2017**, *121* (May), 67−75.
(19) Satilmis, B.; Uyar, T. Fabrication of Thermally Crosslinked Hydrolyzed Polymers of Intrinsic Microporosity (HPIM)/Polybenzoxazine Electrospun Nanofibrous Membranes. *Macromol. Chem. Phys.* **2019**, *220* (1), 1−11.
(20) Satilmis, B.; Uyar, T. Removal of Aniline from Air and Water by Polymers of Intrinsic Microporosity (PIM-1) Electrospun Ultrafine Fibers. *J. Colloid Interface Sci.* **2018**, *516*, 317−324.
(21) Pan, Y.; Zhang, L.; Li, Z.; Ma, L.; Zhang, Y.; Wang, J.; Meng, J. Hierarchical Porous Membrane via Electrospinning PIM-1 for Micropollutants Removal. *Appl. Surf. Sci.* **2018**, *443*, 441−451.
(22) Ranjith, K. S.; Satilmis, B.; Uyar, T. Hierarchical Electrospun PIM Nanofibers Decorated with ZnO Nanorods for Effective Pollutant Adsorption and Photocatalytic Degradation. *Mater. Today* **2018**, *21* (9), 989−990.
(23) Satilmis, B.; Uyar, T. Development of Superhydrophobic Electrospun Fibrous Membrane of Polymers of Intrinsic Microporosity (PIM-2). *Eur. Polym. J.* **2019**, *112*, 87−94.
(24) Satilmis, B.; Uyar, T. Amine Modified Electrospun PIM-1 Ultrafine Fibers for an Efficient Removal of Methyl Orange from an Aqueous System. *Appl. Surf. Sci.* **2018**, *453* (May), 220−229.
(25) Satilmis, B.; Isık, T.; Demir, M. M.; Uyar, T. Amidoxime Functionalized Polymers of Intrinsic Microporosity (PIM-1) Electrospun Ultrafine Fibers for Rapid Removal of Uranyl Ions from Water. *Appl. Surf. Sci.* **2019**, *467−468*, 648−657.
(26) Zhang, F.; Ma, Y.; Liao, J.; Breedveld, V.; Lively, R. P. Solution-Based 3D Printing of Polymers of Intrinsic Microporosity. *Macromol. Rapid Commun.* **2018**, *39* (13), 1800274.
(27) Arey, B. W.; Christ, J. F.; Barrett, C. A.; Zhong, L.; Kennedy, Z. C. Tunable Porosity in Fused Filament 3D-Printed Blends of Intrinsically Porous Polymer (PIM-1) and Thermoplastic Aliphatic Polyesters (PCL and PLA). *ACS Appl. Polym. Mater.* **2019**, *1*, 482.
(28) Li, D.; Xia, Y. Electrospinning of Nanofibers: Reinventing the Wheel? *Adv. Mater.* **2004**, *16* (14), 1151−1170.
(29) Ramakrishna, S.; Fujihara, K.; Teo, W. E.; Yong, T.; Ma, Z.; Ramaseshan, R. Electrospun Nanofibers: Solving Global Issues. *Mater. Today* **2006**, *9* (3), 40−50.
(30) Greiner, A.; Wendorff, J. H. Electrospinning: A Fascinating Method for the Preparation of Ultrathin Fibers. *Angew. Chem., Int. Ed.* **2007**, *46* (30), 5670−5703.
(31) Weber, J.; Du, N.; Guiver, M. D. Influence of Intermolecular Interactions on the Observable Porosity in Intrinsically Microporous Polymers. *Macromolecules* **2011**, *44* (7), 1763−1767.
(32) Koombhongse, S.; Liu, W.; Reneker, D. H. Flat Polymer Ribbons and Other Shapes by Electrospinning. *J. Polym. Sci., Part B: Polym. Phys.* **2001**, *39* (21), 2598−2606.
(33) Katsogiannis, K. A. G.; Vladisavljević, G. T.; Georgiadou, S. Porous Electrospun Polycaprolactone (PCL) Fibres by Phase Separation. *Eur. Polym. J.* **2015**, *69*, 284−295.
(34) Pai, C.; Boyce, M. C.; Rutledge, G. C. Morphology of Porous and Wrinkled Fibers of Polystyrene Electrospun from Dimethylformamide. *Macromolecules* **2009**, *42* (6), 2102−2114.
(35) Megelski, S.; Stephens, J. S.; Chase, D. B.; Rabolt, J. F. Micro- and Nanostructured Surface Morphology on Electrospun Polymer Fibers. *Macromolecules* **2002**, *35* (22), 8456−8466.

https://dx.doi.org/10.1021/acsapm.0c00386
ACS Appl. Polym. Mater. XXXX, XXX, XXX−XXX

(36) Casper, C. L.; Stephens, J. S.; Tassi, N. G.; Chase, D. B.; Rabolt, J. F. Controlling Surface Morphology of Electrospun Polystyrene Fibers: Effect of Humidity and Molecular Weight in the Electrospinning Process. *Macromolecules* **2004**, *37* (2), 573−578.
(37) Qi, Z.; Yu, H.; Chen, Y.; Zhu, M. Highly Porous Fibers Prepared by Electrospinning a Ternary System of Nonsolvent/Solvent/Poly(l-Lactic Acid). *Mater. Lett.* **2009**, *63* (3−4), 415−418.
(38) Chen, P. Y.; Tung, S. H. One-Step Electrospinning to Produce Nonsolvent-Induced Macroporous Fibers with Ultrahigh Oil Adsorption Capability. *Macromolecules* **2017**, *50* (6), 2528−2534.
(39) Liu, W.; Huang, C.; Jin, X. Tailoring the Grooved Texture of Electrospun Polystyrene Nanofibers by Controlling the Solvent System and Relative Humidity. *Nanoscale Res. Lett.* **2014**, *9* (1), 350.
(40) Wang, L.; Pai, C. L.; Boyce, M. C.; Rutledge, G. C. Wrinkled Surface Topographies of Electrospun Polymer Fibers. *Appl. Phys. Lett.* **2009**, *94* (15), 151916.
(41) Nayani, K.; Katepalli, H.; Sharma, C. S.; Sharma, A.; Patil, S.; Venkataraghavan, R. Electrospinning Combined with Nonsolvent-Induced Phase Separation to Fabricate Highly Porous and Hollow Submicrometer Polymer Fibers. *Ind. Eng. Chem. Res.* **2012**, *51* (4), 1761−1766.
(42) Bognitzki, M.; Czado, W.; Frese, T.; Schaper, A.; Hellwig, M.; Steinhart, M.; Greiner, A.; Wendorff, J. H. Nanostructured Fibers via Electrospinning. *Adv. Mater.* **2001**, *13* (1), 70−72.
(43) Gupta, A.; Saquing, C. D.; Afshari, M.; Tonelli, A. E.; Khan, S. A.; Kotek, R. Porous Nylon-6 Fibers via a Novel Salt-Induced Electrospinning Method. *Macromolecules* **2009**, *42* (3), 709−715.
(44) Ji, L.; Lin, Z.; Medford, A. J.; Zhang, X. Porous Carbon Nanofibers from Electrospun Polyacrylonitrile/SiO_2 Composites as an Energy Storage Material. *Carbon* **2009**, *47* (14), 3346−3354.
(45) Im, J. S.; Jang, J.; Lee, Y. Synthesis and Characterization of Mesoporous Electrospun Carbon Fibers Derived from Silica Template. *J. Ind. Eng. Chem.* **2009**, *15* (6), 914−918.
(46) Natarajan, L.; New, J.; Dasari, A.; Yu, S.; Manan, M. A. Surface Morphology of Electrospun PLA Fibers: Mechanisms of Pore Formation. *RSC Adv.* **2014**, *4* (83), 44082−44088.
(47) Fashandi, H.; Karimi, M. Pore Formation in Polystyrene Fiber by Superimposing Temperature and Relative Humidity of Electrospinning Atmosphere. *Polymer* **2012**, *53* (25), 5832−5849.
(48) Yu, X.; Xiang, H.; Long, Y.; Zhao, N.; Zhang, X.; Xu, J. Preparation of Porous Polyacrylonitrile Fibers by Electrospinning a Ternary System of PAN/DMF/H2O. *Mater. Lett.* **2010**, *64* (22), 2407−2409.
(49) Rezabeigi, E.; Sta, M.; Swain, M.; McDonald, J.; Demarquette, N. R.; Drew, R. A. L.; Wood-Adams, P. M. Electrospinning of Porous Polylactic Acid Fibers during Nonsolvent Induced Phase Separation. *J. Appl. Polym. Sci.* **2017**, *134* (20).
(50) Budd, P. M.; Elabas, E. S.; Ghanem, B. S.; Makhseed, S.; McKeown, N. B.; Msayib, K. J.; Tattershall, C. E.; Wang, D. Solution-Processed, Organophilic Membrane Derived from a Polymer of Intrinsic Microporosity. *Adv. Mater.* **2004**, *16* (5), 456−459.
(51) Jue, M. L.; McKay, C. S.; McCool, B. A.; Finn, M. G.; Lively, R. P. Effect of Nonsolvent Treatments on the Microstructure of PIM-1. *Macromolecules* **2015**, *48* (16), 5780−5790.
(52) Jue, M. L.; McKay, C. S.; McCool, B. A.; Finn, M. G.; Lively, R. P. Effect of Nonsolvent Treatments on the Microstructure of PIM-1. *Macromolecules* **2015**, *48*, 5780−5790.
(53) Ogieglo, W.; Ghanem, B.; Pinnau, I.; Wessling, M. How Much Do Ultrathin Polymers with Intrinsic Microporosity Swell in Liquids? *J. Phys. Chem. B* **2016**, *120* (39), 10403−10410.
(54) Guenthner, A. J.; Khombhongse, S.; Liu, W.; Dayal, P.; Reneker, D. H.; Kyu, T. Dynamics of Hollow Nanofiber Formation During Solidification Subjected to Solvent Evaporation. *Macromol. Theory Simul.* **2006**, *15* (1), 87−93.
(55) Pauchard, L.; Allain, C. Buckling Instability Induced by Polmer Solution Drying. *Europhys. Lett.* **2003**, *62* (6), 897.
(56) Du, L.; Xu, H.; Zhang, Y.; Zou, F. Electrospinning of Polycaprolatone Nanofibers with DMF Additive: The Effect of Solution Proprieties on Jet Perturbation and Fiber Morphologies. *Fibers Polym.* **2016**, *17* (5), 751−759.
(57) Lee, K. H.; Kim, H. Y.; La, Y. M.; Lee, D. R.; Sung, N. H. Influence of a Mixing Solvent with Tetrahydrofuran AndN,N-Dimethylformamide on Electrospun Poly(Vinyl Chloride) Nonwoven Mats. *J. Polym. Sci., Part B: Polym. Phys.* **2002**, *40* (19), 2259−2268.
(58) Hsu, C.; Shivkumar, S. N,N-Dimethylformamide Additions to the Solution for the Electrospinning of Poly(ε-Caprolactone) Nanofibers. *Macromol. Mater. Eng.* **2004**, *289* (4), 334−340.
(59) Sun, Z.; Deitzel, J. M.; Knopf, J.; Chen, X.; Gillespie, J. W. The Effect of Solvent Dielectric Properties on the Collection of Oriented Electrospun Fibers. *J. Appl. Polym. Sci.* **2012**, *125* (4), 2585−2594.
(60) Gu, X.; Song, X.; Shao, C.; Zeng, P.; Lu, X.; Shen, X.; Yang, Q. Electrospinning of Poly(Butylene-Carbonate): Effect of Solvents on the Properties of the Nanofibers Film. *Int. J. Electrochem. Sci.* **2014**, *9* (12), 8045−8056.
(61) Smallwood, I. M. *Handbook of Organic Solvent Properties*; Elsevier, 1996.
(62) van de Witte, P.; Dijkstra, P. J.; van den Berg, J. W. A.; Feijen, J. Phase Separation Processes in Polymer Solutions in Relation to Membrane Formation. *J. Membr. Sci.* **1996**, *117* (1−2), 1−31.
(63) Tripathi, A.; Rutkevičius, M.; Bose, A.; Rojas, O. J.; Khan, S. A. Experimental and Predictive Description of the Morphology of Wet-Spun Fibers. *ACS Appl. Polym. Mater.* **2019**, *1* (6), 1280−1290.
(64) Jeromenok, J.; Weber, J. Restricted Access: On the Nature of Adsorption/Desorption Hysteresis in Amorphous, Microporous Polymeric Materials. *Langmuir* **2013**, *29* (42), 12982−12989.
(65) Kupgan, G.; Liyana-Arachchi, T. P.; Colina, C. M. NLDFT Pore Size Distribution in Amorphous Microporous Materials. *Langmuir* **2017**, *33* (42), 11138−11145.
(66) Pang, S. H.; Jue, M. L.; Leisen, J.; Jones, C. W.; Lively, R. P. PIM-1 as a Solution-Processable "Molecular Basket" for CO_2 Capture from Dilute Sources. *ACS Macro Lett.* **2015**, *4* (12), 1415−1419.
(67) Yu, C. H.; Huang, C. H.; Tan, C. S. A Review of CO_2 Capture by Absorption and Adsorption. *Aerosol Air Qual. Res.* **2012**, *12* (5), 745−769.
(68) Landaverde-Alvarado, C.; Morris, A. J.; Martin, S. M. Gas Sorption and Kinetics of CO_2 Sorption and Transport in a Polymorphic Microporous MOF with Open Zn (II) Coordination Sites. *J. CO2 Util.* **2017**, *19*, 40−48.
(69) Ho, Y.S; McKay, G Pseudo-Second Order Model for Sorption Processes. *Process Biochem.* **1999**, *34* (5), 451−465.

https://dx.doi.org/10.1021/acsapm.0c00386
ACS Appl. Polym. Mater. XXXX, XXX, XXX−XXX